Carbon Resources Conversion 4 (2021) 205–213

Contents lists available at ScienceDirect

Carbon Resources Conversion

journal homepage: www.sciencedirect.com/journal/carbon-resources-conversion

Comparative study of $MCe_{0.75}Zr_{0.25}O_y$ (M = Cu, Mn, Fe) catalysts for selective reduction of NO by CO: Activity and reaction pathways

Junyao He [a,b], Running Kang [a,c], Xiaolin Wei [a,c], Junqin Huang [a,c], Feng Bin [a,c,*], Kwun Nam Hui [d], Kwan San Hui [e], Dongyin Wu [b,*]

[a] State Key Laboratory of High-Temperature Gas Dynamics, Institute of Mechanics, Chinese Academy of Sciences, Beijing 100190, PR China
[b] School of Energy and Power Engineering, Xi'an Jiaotong University, 710049 Xi'an, PR China
[c] School of Engineering Science, University of Chinese Academy of Sciences, 100049 Beijing, PR China
[d] Institute of Applied Physics and Materials Engineering, University of Macau, Avenida da Universidade, Taipa, Macau, PR China
[e] School of Engineering, Faculty of Science, University of East Anglia, Norwich Research Park, NR4 7TJ, United Kingdom

ARTICLE INFO

Keywords:
CO-SCR
Catalytic combustion
Oxygen species
Synergistic removal
Reaction mechanism

ABSTRACT

Basic oxygen furnace steelmaking leads to the production of CO-rich off-gas. When CO and NO are combined in off-gas, selective catalytic reduction by CO (CO-SCR) effectively achieves the synergistic removal of both pollutants. In this paper, $CuCe_{0.75}Zr_{0.25}O_y$, $MnCe_{0.75}Zr_{0.25}O_y$, and $FeCe_{0.75}Zr_{0.25}O_y$ catalysts are prepared and evaluated for their CO-SCR activity, and the results show that the reaction system needs to be anaerobic; thus, the CO-SCR reaction can be dominant. The T_{90} values of $CuCe_{0.75}Zr_{0.25}O_y$ and $FeCe_{0.75}Zr_{0.25}O_y$ are 200 °C and 223 °C, respectively. The activities of these two catalysts are higher than that of $MnCe_{0.75}Zr_{0.25}O_y$ (T_{90} = 375 °C). Linear nitrate and bridged bidentate nitrate are the main intermediate species involved in NO conversion on the catalyst surface, and bidentate CO_3^{2-} coordination is the main intermediate species involved in CO conversion on the catalyst surface. $CuCe_{0.75}Zr_{0.25}O_y$ has high lattice oxygen mobility and is more likely to react with NO and CO. In the presence of oxygen, most CO is oxidized by O_2, which increases continuously to 100%, 100%, and 98% for $CuCe_{0.75}Zr_{0.25}O_y$, $FeCe_{0.75}Zr_{0.25}O_y$, and $MnCe_{0.75}Zr_{0.25}O_y$, respectively; additionally, CO is oxidized by O_2, and the CO-SCR reaction cannot be carried out.

1. Introduction

Basic oxygen furnace (BOF) steelmaking has been widely employed as an efficient technology to produce good-quality steel from pig iron, where a supersonic jet of pure oxygen is blown from the top into the metal bath at a high speed to elevate the temperature to promote the intense reactions of decarburization and combustion [1]. As a consequence, the off-gas produced from steelmaking contains a column of mostly carbon monoxide (CO) and some carbon dioxide (CO_2), which emerges from the mouth of the converter. The off-gas produced during steelmaking intermissions is first cooled by a gasification cooling stack coupled with water spray to remove the residual sensible heat and then discharged into the atmosphere via a direct fired burner because the CO concentration is relatively low, and explosions occur easily in the CO/O_2 mixture [2].

The increased pressures of profitability and environmental concerns have triggered awareness of potential technologies that could utilize CO-rich off-gas [3]. The typical method is post-combustion of CO induced by air, which takes place inside the bath or prior to reaching the gasification cooling stack. Unfortunately, the combustion temperatures may exceed 1800 ℃ [4,5], leading to dissociation reactions in the post combustion zone that yield thermal nitrogen oxides (NO_x) as a secondary pollutant [6]. Selective catalytic reduction is currently accepted for NO_x removal from stationary sources, requiring the use of ammonia (NH_3) as a reducing agent [7,8]. NH_3 is a toxic gas with a risk of chemical accidents during storage and transportation. By comparison, CO in the converter off-gas is not effectively removed, which poses a certain safety hazard. The selective catalytic reduction of NO_x by CO (CO-SCR) is expected because of the coexistence of CO and NO_x in off-gas [9–11]. Such a technology can simultaneously remove two kinds of waste gas without using NH_3, which avoids the initial investment cost of NH_3 injection technology transformation and the potential risk

* Corresponding authors at: State Key Laboratory of High-Temperature Gas Dynamics, Institute of Mechanics, Chinese Academy of Sciences, Beijing 100190, PR China (Feng Bin).
E-mail addresses: binfeng@imech.ac.cn (Feng Bin), dongyinwu@mail.xjtu.edu.cn (D. Wu).

https://doi.org/10.1016/j.crcon.2021.07.002
Received 4 March 2021; Received in revised form 29 June 2021; Accepted 5 July 2021
Available online 10 July 2021

brought by NH_3. Thus, it has research value and importance.

Catalysts employed in CO-SCR mainly include noble metal oxides and transition metal oxides. Researchers have focused on Ir-based noble metal catalysts. Under the condition of low oxygen (1% O_2), Ogura et al. [12] proved that NO is selectively reduced by CO on Ir/SiO_2 in an oxidizing atmosphere containing 1%–10% O_2 within the temperature range of 300 °C–500 °C. According to Doi et al. [13], Ir/SiO_2 and Ir/CeO_2 are the catalysts with the highest and lowest activity, respectively, among all the catalysts tested because the effect of the silica support stabilizes the Ir species in the active reducing state produced in the reaction via Ir-carrier synergism. Inomata et al. [14] compared the CO-SCR activity of Ir-based catalysts using metallic oxides as supports, and the results indicated that Ir/WO_3 exhibits a better denitrification activity than Ir/SiO_2, Ir/Nb_2O_5, and Ir/Ta_2O_5 catalysts at low temperature. Although several noble metal catalysts have good catalytic activity for CO-SCR, their high cost and poor high-temperature resistance limit their wide use in industry. Therefore, studying transition metal catalysts with high activity to develop CO-SCR technology is an important research direction [15,16].

Owing to the considerable catalytic activity and stability of cerium-based composite oxides, they have been recognized as substitutes for precious metals in SCR [17–19]. Liu et al. [20] proposed that the dispersion of active sites can be enhanced by CeO_2. Guo et al. [21] showed that a Ce-doped Ni-Al-O_x catalyst has excellent CO-SCR performance. At a doping amount of 20%, the NO conversion can reach 95% at 250 °C. Dong et al. [22] showed that the Fe^{2+} of the Fe_2O_3-CeO_2/$Ti_{0.5}Sn_{0.5}O_2$ catalyst is the main active site for CO-SCR. Copper is rich in electrons, as the d-orbitals are almost completely occupied by electrons [23]. Hence, copper ions are prone to constitute a stabilized bond with CO and exhibit excellent CO adsorption properties. The Cu_x/CeO_2-Fe_2O_3 (Cu_x/CF) catalyst was studied by Cheng et al. [24], where copper oxide is an active component of Cu_x/CF. Kong et al. [25] developed a CuMn-CeLa-O/γ-Al_2O_3 catalyst, which showed that Ce or La doping can enhance the structural defects of CuO and MnO_x, resulting in more oxygen vacancies and improving the activity of catalysts. In an activity experiment of CuO/MnO_x-γ-Al_2O_3 catalysts, the support Mn/Al ratio and manganese oxidation state had remarkable influences on the CO-SCR activity [26]. However, most transition metal catalysts are still tested under oxygen-free conditions, and discussion on the influence mechanism of Ce solid solution in CO-SCR reaction is rare. No relevant report is available on the synergistic effect of active components such as Cu, Mn, and Fe as independent active sites and the Ce support.

To clarify the catalytic performance of transition metal catalysts in aerobic environments and the surface reaction mechanism of Ce solid solution catalysts, $CuCe_{0.75}Zr_{0.25}O_y$, $MnCe_{0.75}Zr_{0.25}O_y$, and $FeCe_{0.75}Zr_{0.25}O_y$ catalysts were prepared in this paper. Their physicochemical properties and catalytic activity were studied, and the characterization technologies included X-ray diffraction (XRD), Raman spectroscopy, X-ray photoelectron spectroscopy (XPS), temperature-programmed reduction of hydrogen (H_2-TPR), and CO– and O_2-temperature-programmed desorption (TPD). The reaction intermediates were also studied by infrared (IR) spectrum analysis. The good activity of $CuCe_{0.75}Zr_{0.25}O_y$ suggests that the impregnation of copper oxides on the surface of Ce-Zr solid solutions is a feasible strategy for designing an industrial catalyst for CO-SCR that would be helpful for pollutant removal in the iron and steel industry.

2. Experimental specifications

2.1. Catalyst preparation

$CuCe_{0.75}Zr_{0.25}O_y$, $MnCe_{0.75}Zr_{0.25}O_y$, and $FeCe_{0.75}Zr_{0.25}O_y$ catalysts were synthesized by the sol–gel method. With respect to $CuCe_{0.75}Zr_{0.25}O_y$, $Cu(NO_3)_2{\cdot}3H_2O$, $Ce(NO_3)_3{\cdot}6H_2O$, and $Zr(NO_3)_4{\cdot}5H_2O$ nitrates were mixed in 400 mL of absolute ethanol and then placed in a magnetic mixer, where the Cu:Ce:Zr molar ratio of 4:3:1 was determined based on the optimization of the structure and activity from our previously published work [27]. Bacterial cellulose was used as the pore-forming agent for the catalysts. Five grams of bacterial cellulose was dissolved in the current solution and then stirred at constant temperature (50 °C recommended) until the gel formed. It was then cooled to room temperature, and the time required for the aging of the catalyst was 48 h. Then, the catalysts were dried at 80 °C for 12 h and then calcined at 550 °C for 4 h in a muffle furnace. Unlike the $Ce_{0.75}Zr_{0.25}O_y$ and pure CeO_2 that were prepared as reference samples, to guarantee validity and reliability, $MnCe_{0.75}Zr_{0.25}O_y$ and $FeCe_{0.75}Zr_{0.25}O_y$ catalysts with Mn:Ce:Zr or Fe:Ce:Zr molar ratios of 4:3:1 were prepared according to the same procedure that was used to prepare $CuCe_{0.75}Zr_{0.25}O_y$. The elemental contents of the catalysts were analyzed by X-ray fluorescence spectrometry (XRF), and the results are shown in Table 1.

Table 1
Element contents of catalysts detected by XRF.

Catalyst	M (M = Cu, Mn, Fe)/wt%	Ce/wt%	Zr/wt%
$CuCe_{0.75}Zr_{0.25}O_y$	30.79	52.17	13.53
$MnCe_{0.75}Zr_{0.25}O_y$	27.95	52.24	13.49
$FeCe_{0.75}Zr_{0.25}O_y$	26.29	54.59	14.06

2.2. Characterization

The catalyst sample was measured by XRD using a DX-2700 X-ray diffractometer (Cu Kα radiation, λ = 0.1541 nm, X-ray tube voltage: 40 kV, X-ray tube current: 30 Ma, scanning step: 0.06°, angle range: 10°–85°, and scanning speed: 2°/min). Raman spectra were acquired using a HORIBA LabRAM HR Evolution spectrometer (HSES with 100 nm steps). XPS was carried out using a Perkin–Elmer PHI-1600 ESCA X-ray photoelectron spectrometer. The X-ray source was a Mg anode target (350 eV), and C 1 s (Eb = 284.8 eV) was used as the internal standard to correct the binding energy of each species. A TP-5080B auto multiple-purpose sorption instrument (Tianjin Xianquan Co. Ltd., China) was used to carry out H_2-TPR. For each experiment, a 30 mg sample was placed into a quartz reactor and out-gassed by pure He at 300 °C for 0.5 h. Then, the test sample was cooled to 40 °C followed by flowing 5% H_2/He, and the H_2-TPR measurement was recorded with a heating rate of 10 °C/min and a final temperature of 1000 °C. CO– and NO-TPD were also performed on the same instrument. Then, 5%/He CO or 5%/He NO was adsorbed for 0.5 h after the pretreatment of each sample (30 mg) with pure He. The adsorption temperature was 50 °C, and the samples were exposed to N_2 flow to remove physically adsorbed O_2 or CO until the baseline was stable. The testing temperature was then raised from 50 °C to 1000 °C with a heating rate of 10 °C/min. H_2, CO, and NO consumption was quantitatively calculated by time integration of the TPR and TPD profiles. In situ IR spectra were recorded on a Tensor 27 IR spectrometer. Next, 15 mg of catalyst powder was prepared in thin self-standing wafers and inserted in a heatable holder of the cell. After the pretreatment of each sample by He, a spectrum was taken for use as a background.

After our on-site measurement of off-gas composition, the CO concentration is approximately 5%-15%, and the concentrations of NO (approximately 1.2%) and O_2 (approximately 0.5%) are very low in the off gases. Under our experimental conditions, the composition of the experimental gas was determined to be 1%NO + 5%CO + 1%O_2 with He as the balance gas. Each gas was drained into the gas mixing unit via a separate pipeline. After the gas was fully mixed, it entered the in situ reaction cell from the main pipe. Each pipe was equipped with separate mass flow controllers, and the total rate of flow into the in situ reaction cell was 40 mL/min. A series of time-dependent IR spectra was used during SCR for each temperature interval (30 °C–400 °C).

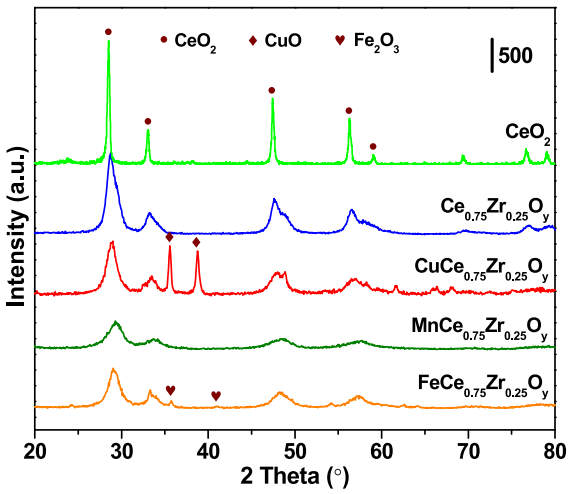

Fig. 1. XRD patterns of pure CeO_2, $Ce_{0.75}Zr_{0.25}O_y$, $CuCe_{0.75}Zr_{0.25}O_y$, $MnCe_{0.75}Zr_{0.25}O_y$, and $FeCe_{0.75}Zr_{0.25}O_y$ catalysts. The samples were calcined at 550 °C for 4 h.

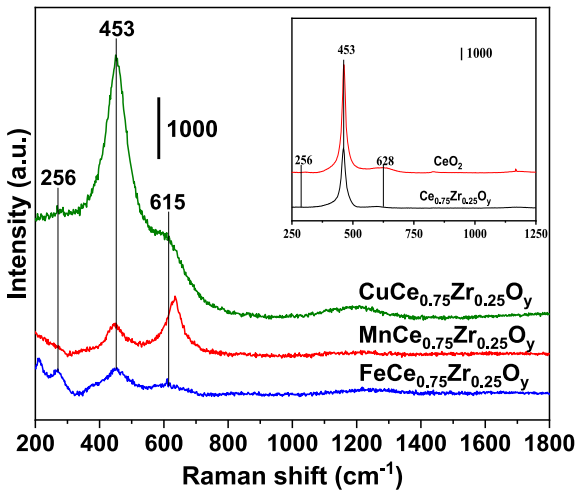

Fig. 2. Raman spectra of pure CeO_2, $Ce_{0.75}Zr_{0.25}O_y$, $CuCe_{0.75}Zr_{0.25}O_y$, $MnCe_{0.75}Zr_{0.25}O_y$, and $FeCe_{0.75}Zr_{0.25}O_y$ catalysts. The samples were calcined at 550 °C for 4 h.

2.3. Catalytic activity testing

The CO-SCR activity of the powder-type catalysts was evaluated in a fixed-bed quartz microreactor with an inner diameter of 4 mm. The catalysts were passed through a sieve to obtain grains sized 20–40 mesh, placed at the center of the reactor (0.2 g), and packed with quartz wool on both sides. The temperature information of the catalytic bed was fed back by a K-type thermocouple. Mass flow controllers were used to control the feed gas flow ($NO + CO + O_2$/He), and the total gas flow rate was fixed at 200 standard cubic centimeters per minute. The detection of outlet gas composition was completed by an online gas analyzer (Maihak). The gas analyzer was customized for different test gases, and each detector was connected in series to detect the tail gas. Reaction conversion was calculated as follows:

$$Con.(\%) = \frac{c_{in} - c_{out}}{c_{in}} \times 100\%$$

With respect to CO removal, c_{in} is the CO concentration at the inlet of the reactor, c_{out} is the CO concentration outlet of the reactor, and the concentration range of the CO detector was 0–20%. For the NO removal, the concentration range of the NO detector was 0–500 ppm, c_{in} and c_{out} stand for the NO concentrations at the inlet and outlet of the reactor, respectively. All activity tests in this paper were repeated at least twice to ensure reproducibility, and data were recorded only when the SCR reaction reached the steady state after 10 min of continuous operation at each temperature.

3. Results and discussion

3.1. Crystal structure of the solid solution catalyst

Fig. 1 shows the XRD results of the prepared pure CeO_2, $Ce_{0.75}Zr_{0.25}O_y$, $CuCe_{0.75}Zr_{0.25}O_y$, $MnCe_{0.75}Zr_{0.25}O_y$, and $FeCe_{0.75}Zr_{0.25}O_y$ catalysts, which present typical features of cubic fluorite-type CeO_2 crystals (JCPDS 34–0394). The diffraction angles of the peaks for $Ce_{0.75}Zr_{0.25}O_y$ are broadened compared with those of CeO_2. A careful comparison of the peak positions of the respective angle values shows that $Ce_{0.75}Zr_{0.25}O_y$ peak slightly shifts to higher angles. The reason for this phenomenon is that these zirconium cations are well doped into the lattice of CeO_2 to form a uniform solid solution. A slight shift in the diffraction peaks of $Ce_{0.75}Zr_{0.25}O_y$ can also be detected in the XRD patterns of $CuCe_{0.75}Zr_{0.25}O_y$, $MnCe_{0.75}Zr_{0.25}O_y$, and $FeCe_{0.75}Zr_{0.25}O_y$. Unlike that of $MnCe_{0.75}Zr_{0.25}O_y$, the spectra of the $CuCe_{0.75}Zr_{0.25}O_y$ and $FeCe_{0.75}Zr_{0.25}O_y$ catalysts clearly show the characteristic peaks of bulk CuO (35.5° and 38.7°, JCPDS 80-1268) and Fe_2O_3 (33.2° and 54.1°, JCPDS 33-0664), respectively. No diffraction peaks related to manganese and metal oxides are detected for $MnCe_{0.75}Zr_{0.25}O_y$, indicating that these metal species are well dispersed and exist in the form of amorphous nanoparticles on the surface. The XRD results reveal that copper, manganese, and iron are effectively inserted into the cerium–zirconium solid solution, which contributes to the strong interaction among them.

3.2. Raman spectroscopy

Raman spectroscopy was employed to obtain surface information about the catalysts to compensate for the lack of XRD data. In Fig. 2, the Raman spectrum of CeO_2 exhibits the main band at 462 cm^{-1}, which corresponds to the F_{2g} symmetry vibration mode of the cubic fluorite-type structure, and this band related to the first-order transition is the only one allowed for a perfect crystal. Two weak peaks at 256 and 615 cm^{-1} are also observed: the former is attributed to the rearrangement of oxygen from the CeO_2 inherent fluorite lattice structure, and the latter is attributed to the nondegenerate LO mode of CeO_2 resulting from relaxation of the symmetry rules, which is often related to oxygen vacancies in the CeO_2 fluorite lattice [28]. Clearly, the characteristic F_{2g} peaks of CeO_2 shift to the left and become broader for $CuCe_{0.75}Zr_{0.25}O_y$, $MnCe_{0.75}Zr_{0.25}O_y$, and $FeCe_{0.75}Zr_{0.25}O_y$. Such shifting occurs because of lattice distortions in CeO_2 arising from copper, manganese, iron, and zirconium addition. The incorporation of these cations into the CeO_2 lattice leads to the formation of solid solutions, with the creation of oxygen vacancies to compensate for the charge discrepancy. The ratio of the areas of the peaks at 615 and 453 cm^{-1} (A_{615}/A_{453}) was semi-quantitatively analyzed for the surface oxygen vacancy concentration in the three catalysts [29], and the results are listed in descending order: $MnCe_{0.75}Zr_{0.25}O_y$ (1.72) > $FeCe_{0.75}Zr_{0.25}O_y$ (0.48) > $CuCe_{0.75}Zr_{0.25}O_y$ (0.29) > $Ce_{0.75}Zr_{0.25}O_y$ (0.28) > CeO_2 (0.04).

3.3. XPS analysis

XPS analyses were carried out to investigate the chemical states and atom concentrations on the surfaces of the catalysts. The Cu $2p_{3/2}$ spectrum of $CuCe_{0.75}Zr_{0.25}O_y$ (Fig. 3a) depicts a broad peak in the range of 928–938 eV, indicative of the presence of various copper species, where the major characteristic of Cu^{2+} is a shake-up peak of 938–946 eV. Deconvolution performed on the peak shows that the characteristic peak of Cu $2p_{3/2}$ can be well fitted by two peaks corresponding to Cu^+ at 933.0 eV and Cu^{2+} at 934.3 eV with a Cu^+:Cu^{2+} atomic ratio of 0.52. In

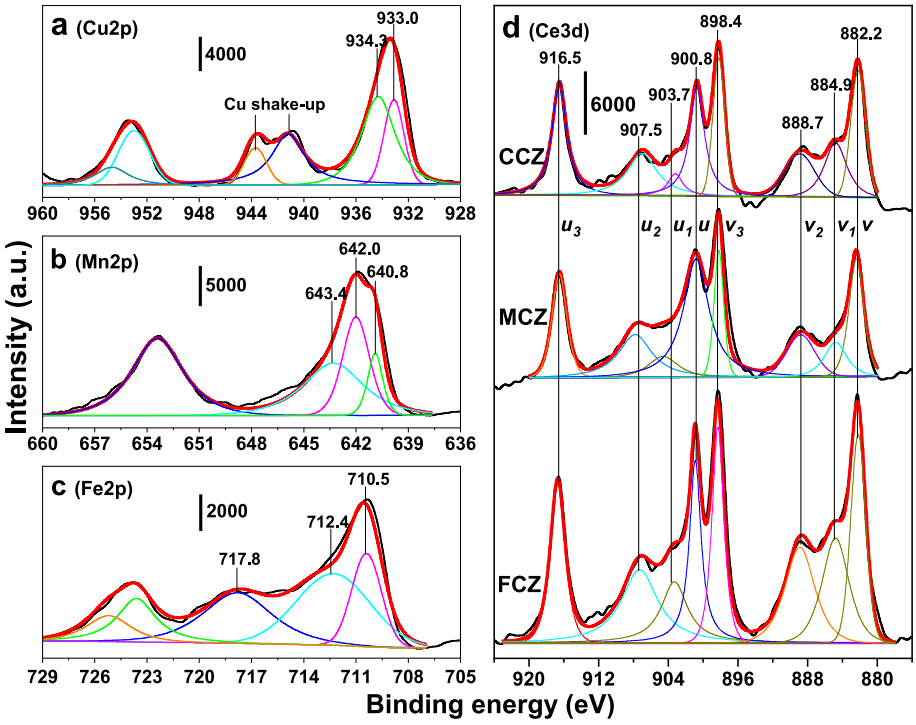

Fig. 3. XPS narrow spectra of Cu 2p (a), Mn 2p (b), Fe 2p (c), and Ce 3d (d) over the $CuCe_{0.75}Zr_{0.25}O_y$, $MnCe_{0.75}Zr_{0.25}O_y$, and $FeCe_{0.75}Zr_{0.25}O_y$ catalysts. Crude line: original data; Smooth line: fitted data.

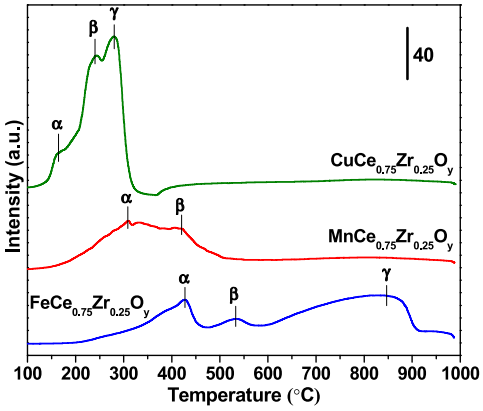

Fig. 4. H_2-TPR profiles of $CuCe_{0.75}Zr_{0.25}O_y$, $MnCe_{0.75}Zr_{0.25}O_y$, and $FeCe_{0.75}Zr_{0.25}O_y$ catalysts. Pretreatment: pure He at 300 °C for 30 min; Sample quality: 30 mg; Experimental conditions: 5% H_2/He (30 mL/min), heating rate 10 °C/min from 50 °C–1000 °C.

the spectrum of $MnCe_{0.75}Zr_{0.25}O_y$, the Mn $2p_{3/2}$ peak (Fig. 3b) can be deconvoluted into three peaks, corresponding to peaks at 640.8, 642.0, and 643.4 eV, which indicates that the manganese is in the oxidation states of + 2, +3, and + 4 [30] with a Mn^{2+}:Mn^{3+}:Mn^{4+} ratio of 1:3.6:2.8. Fig. 3c shows the high-resolution Fe 2p XP spectra of $FeCe_{0.75}Zr_{0.25}O_y$. The peaks at 711 and 725 eV are attributed to Fe $2p_{3/2}$ and Fe $2p_{1/2}$, respectively, and the typical peak at 720 eV related to Fe $2p_{3/2}$ is attributed to the presence of Fe^{3+} [31]. Hence, the Fe $2p_{3/2}$ XPS spectra can be fitted to two peaks: the peak with a binding energy at approximately 710.5 eV is derived from the iron species in FeO form, whereas that at 712.4 eV is attributed to the Fe_3O_4 species. The complexity of the Ce3d spectrum is a consequence of the hybridization between the Ce 4f levels and the O 2p states. In Fig. 3d, the peaks denoted as *v* correspond to Ce $3d_{5/2}$ spin–orbit components, and those categorized as *u* represent the Ce $3d_{3/2}$ spin–orbit components. The Ce^{4+} spectrum was fitted with six peaks at binding energies of *v* (882.2 eV), v_2 (888.7 eV), v_3 (898.4 eV), *u* (900.8 eV), u_2 (907.5 eV), and u_3 (916.5 eV). The XPS signal of Ce^{3+} was deconvoluted into two peaks with binding energies at v_1 (884.9 eV) and u1 (903.7 eV). Quantitative data show that the Ce^{3+}/Ce^{4+} ratios for $CuCe_{0.75}Zr_{0.25}O_y$, $MnCe_{0.75}Zr_{0.25}O_y$, and $FeCe_{0.75}Zr_{0.25}O_y$ were 0.158, 0.164, and 0.282, respectively. The presence of higher Ce^{3+} surface species illustrates the increment of surface oxygen vacancies over the catalysts. Thus, the quantitative data agree with those obtained by Raman analysis.

3.4. Temperature-programmed analysis of catalysts

H_2-TPR was employed to investigate the redox behavior of the

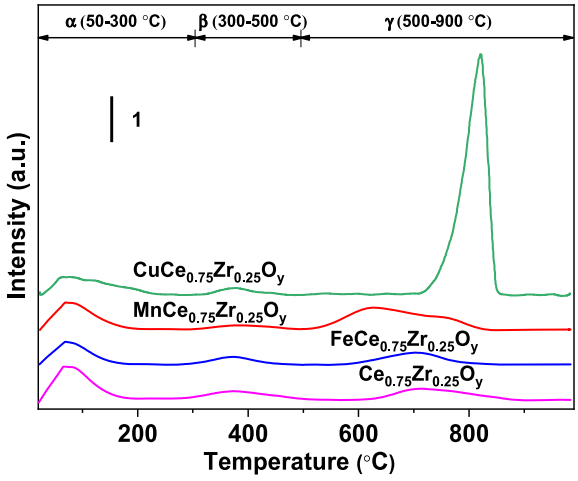

Fig. 5. O_2-TPD profiles of $CuCe_{0.75}Zr_{0.25}O_y$, $MnCe_{0.75}Zr_{0.25}O_y$, and $FeCe_{0.75}Zr_{0.25}O_y$ catalysts. Pretreatment: pure He at 300 °C for 30 min; sample quality: 30 mg; experimental conditions: 5% O_2/He (30 mL/min), heating rate 10 °C/min from 50 °C–1000 °C.

Table 2
Oxygen desorption capacity of the catalysts.

Catalyst	α (μmol/g)	β (μmol/g)	γ (μmol/g)	Total (μmol/g)
$CuCe_{0.75}Zr_{0.25}O_y$	508	88	1939	2535
$MnCe_{0.75}Zr_{0.25}O_y$	532	63	712	1307
$FeCe_{0.75}Zr_{0.25}O_y$	375	59	135	569
$Ce_{0.75}Zr_{0.25}O_y$	544	97	55	696

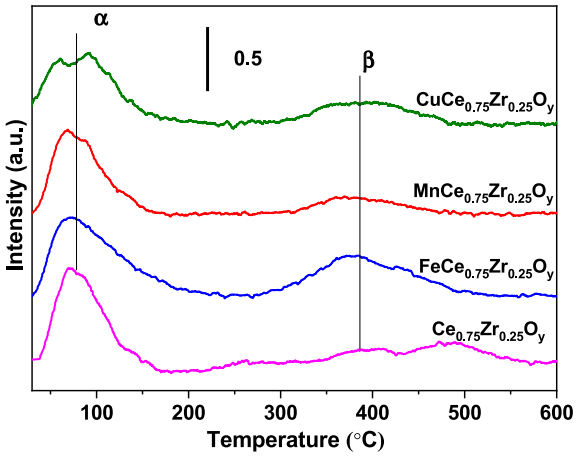

Fig. 6. CO-TPD profiles of $CuCe_{0.75}Zr_{0.25}O_y$, $MnCe_{0.75}Zr_{0.25}O_y$, and $FeCe_{0.75}Zr_{0.25}O_y$ catalysts. Pretreatment: pure He at 300 °C for 30 min; sample quality: 30 mg; experimental conditions: 5% CO/He (30 mL/min), heating rate 10 °C/min from 50 °C–1000 °C.

catalysts, and the results are displayed in Fig. 4. The catalysts were categorized based on their reduction temperatures. Within the range of reducing temperatures, the profile of $CuCe_{0.75}Zr_{0.25}O_y$ exhibits three peaks: α (163 °C), β (240 °C), and γ (280 °C). The low-temperature α peak suggests its enhanced catalytic reducibility, which can probably be attributed to numerous copper ions being incorporated into cerium to form a solid solution, thus weakening the Cu–O and Ce-O bonds. The β peaks can be attributed to the reduction of highly dispersed CuO_x nanoclusters with a smaller size, whereas the γ peak is due to the reduction of crystalline CuO that has been detected by XRD. A similar curve with three reduction peaks can be observed for $FeCe_{0.75}Zr_{0.25}O_y$ but has an evident shift toward higher temperatures than those of $CuCe_{0.75}Zr_{0.25}O_y$, corresponding to α, β, and γ peaks at 427 °C, 532 °C, and 846 °C, respectively. The redox peaks of $MnCe_{0.75}Zr_{0.25}O_y$ are between those of the other catalysts, where the α and β peaks overlap and are located at 308 °C and 419 °C. Through quantitative analysis of the H_2-TPR profiles, H_2 consumption by $CuCe_{0.75}Zr_{0.25}O_y$, $MnCe_{0.75}Zr_{0.25}O_y$, and $FeCe_{0.75}Zr_{0.25}O_y$ was determined to be 1.9, 1.3, and 2.7 mmol/g, respectively.

To further explore the surface oxygen species that participate in the redox reactions, O_2-TPD was performed. Fig. 5 shows that the α peak can be attributed to the desorption of physically adsorbed oxygen (O_{ap}) on the surface at low temperatures. The β peak in the range of 300 °C–500 °C is due to the desorption of chemically adsorbed species (O_{ac}), which may be associated with surface oxygen defects of the solid solution and agrees with the XRD and Raman results. The α and β desorption peaks demonstrate the latent possibility that these species participate in redox reactions. The γ peak at a higher temperature (>500 °C) is assigned to the surface lattice oxygen (O_{la}) that separated from the solid solution. Although the desorption temperature of O_{la} for $CuCe_{0.75}Zr_{0.25}O_y$ is 824 °C, which is higher than those for $MnCe_{0.75}Zr_{0.25}O_y$, $FeCe_{0.75}Zr_{0.25}O_y$, and $Ce_{0.75}Zr_{0.25}O_y$, the abundant lattice oxygen (1.939 mmol/g, Table 2) can be reduced at low temperatures. Therefore, the role that O_{la} plays in redox reactions should be further investigated.

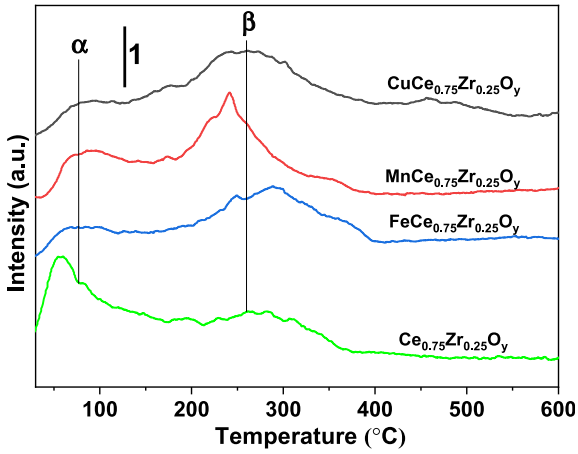

Fig. 7. NO-TPD profiles of $CuCe_{0.75}Zr_{0.25}O_y$, $MnCe_{0.75}Zr_{0.25}O_y$, and $FeCe_{0.75}Zr_{0.25}O_y$ catalysts. Pretreatment: pure He at 300 °C for 30 min; Sample quality: 30 mg; Experimental conditions: 5% NO/He (30 mL/min), heating rate 10 °C/min from 50 °C–1000 °C.

The CO-TPD profiles of the catalysts are shown in Fig. 6. The α peak at approximately 70 °C is attributed to desorption of physically adsorbed CO from the solid solution surface, and the β peak centered within the range of 363 °C–388 °C can be assigned to the desorption of chemically adsorbed CO from the solid solution surface [32]. The bimetallic catalyst has a stronger chemical adsorption capacity for CO. As discussed in relation to the XPS results, the electron density of the active site atom in the bimetallic catalyst increases due to the synergistic effect between metals. $CuCe_{0.75}Zr_{0.25}O_y$ is taken as an example to discuss this phenomenon. In CO adsorption, the d-electron of copper atoms on the surface of solid solution is donated to the unoccupied antibonding π* orbital of CO, forming a d–π backbond with the copper species [33]. Owing to the synergistic effect of bimetals, the proportion of d-π backbonding increases as the d-electron density of surface active species increases. Such a phenomenon can improve the ability of the metal to adsorb CO, strengthening the Cu-C bond. Fig. 3a shows that the desorption peak area on the bimetallic catalyst is larger than that on the monometallic catalyst; hence, the bimetallic catalyst can increase the chemisorption capacity of CO. Similarly, the main driving force of lattice oxygen migration is the oxygen vacancy in the solid solution and the higher surface area [34]. Therefore, among $CuCe_{0.75}Zr_{0.25}O_y$, $MnCe_{0.75}Zr_{0.25}O_y$, and $FeCe_{0.75}Zr_{0.25}O_y$, the β peak of the $CuCe_{0.75}Zr_{0.25}O_y$ catalyst, which has the most oxygen vacancies, tends to shift to the low-temperature region compared with those of the two other catalysts.

Fig. 7 shows the NO-TPD curves. The α peak below 100 °C is the desorption peak of physical NO adsorption, and NO is detected in the tail gas. A small amount of N_2O is also detected in the gas before 250 °C, but the IR absorption peak of N_2O is not observed in the same temperature range in the DRIFT analysis, which is due to the rapid desorption of N_2O and its inability to adsorb on the catalyst surface again [35]. The β peak (240 °C–360 °C) is due to the desorption of NO by chemisorption. In this temperature range, NO is not detected in the tail gas, which may be because NO reacts with lattice oxygen and is then discharged in the form of NO_2 and N_2 [36,37]. The β peak of $CuCe_{0.75}Zr_{0.25}O_y$ shifts to low temperatures compared with those of the two other catalysts. The peak temperature is 240 °C, indicating that $CuCe_{0.75}Zr_{0.25}O_y$, which has high lattice oxygen mobility, is more likely to react with NO. In a comparison of the NO-TPD curves of $CuCe_{0.75}Zr_{0.25}O_y$, $MnCe_{0.75}Zr_{0.25}O_y$, and $FeCe_{0.75}Zr_{0.25}O_y$, the β peak of NO-TPD moves in the low-temperature direction, which indicates that NO reacts with lattice oxygen more easily than CO.

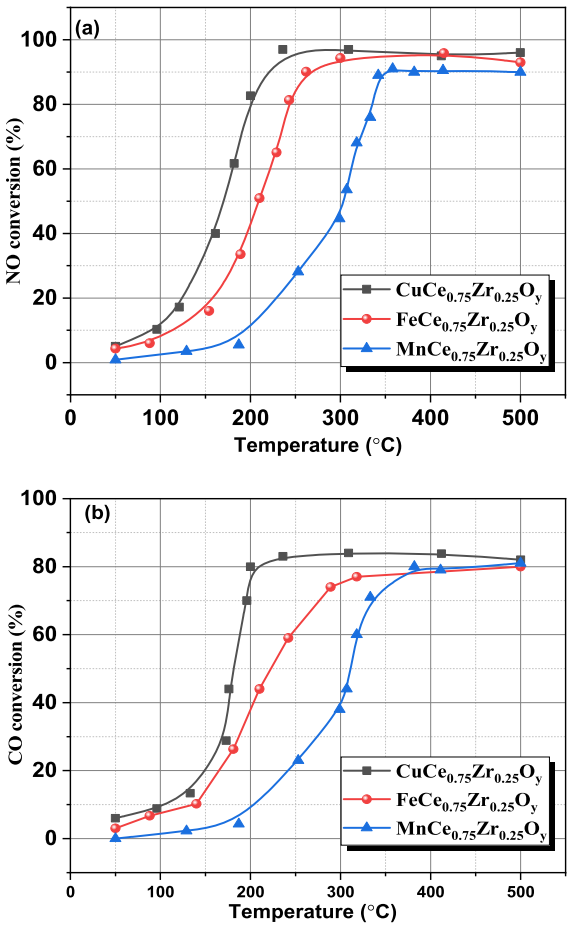

Fig. 8. CO-SCR activity for NO and CO conversions as a function of reaction temperature for $CuCe_{0.75}Zr_{0.25}O_y$, $MnCe_{0.75}Zr_{0.25}O_y$, and $FeCe_{0.75}Zr_{0.25}O_y$ catalysts. Conditions: 0% O_2 + 500 ppm CO + 500 ppm NO/N_2 atmosphere, flow rate: 200 mL/min, weight of catalyst: 0.2 g.

3.5. Catalyst activity

The CO-SCR and CO oxidation reactions were investigated by placing these catalysts in a quartz tube, through which the specific gas flowed. By temperature-programmed control, the temperature was increased from 25 °C to 500 °C at 10 °C/min. The activity testing data results are shown in Fig. 8. $CuCe_{0.75}Zr_{0.25}O_y$ achieved 90% NO conversion at 220 °C (T_{n90}), which is lower than $FeCe_{0.75}Zr_{0.25}O_y$ (T_{n90} = 271 °C) and $MnCe_{0.75}Zr_{0.25}O_y$ (T_{n90} = 351 °C), and CO decreased with the conversion of NO in the activity test.

To further understand the activity of the catalyst in CO-rich off-gas, a CO-rich atmosphere experiment was carried out. CO-SCR is dominant due to the absence of O_2 in the 0% O_2 + 10% CO + 500 ppm NO/N_2 atmosphere (Fig. 9a). $CuCe_{0.75}Zr_{0.25}O_y$ (CCZ) and $FeCe_{0.75}Zr_{0.25}O_y$ (FCZ) achieved 90% NO conversion at 200 °C and 223 °C (T_{n90}), respectively, which are higher than that achieved by $MnCe_{0.75}Zr_{0.25}O_y$ (MCZ, 375 °C). The CO conversion of $CuCe_{0.75}Zr_{0.25}O_y$, $MnCe_{0.75}Zr_{0.25}O_y$, and $FeCe_{0.75}Zr_{0.25}O_y$ is induced at a slow rate, during which the temperature starts at 25 °C and then increases until it reaches 400 °C. During the CO-SCR of CO and NO ($2CO + 2NO \rightarrow 2CO_2 + N_2$), consumption of excess CO arises from its oxidation to yield CO_2 by O_{la} of copper, manganese, and iron species over $CuCe_{0.75}Zr_{0.25}O_y$, $MnCe_{0.75}Zr_{0.25}O_y$, and $FeCe_{0.75}Zr_{0.25}O_y$. CO conversions of $CuCe_{0.75}Zr_{0.25}O_y$ and $MnCe_{0.75}Zr_{0.25}O_y$ occur at temperatures higher than 400 °C because most of the O_{la} has been consumed, whereas an apparent increase can be observed for $FeCe_{0.75}Zr_{0.25}O_y$. O_2-TPD shows that the catalyst gives rise to an O_{la} desorption signal at temperatures > 500 °C, suggesting that the structure of lattice oxygen formed in a solid solution is very stable. A higher temperature is required for the thermal depletion of O_{la}. If a strong reducing agent is present in the experimental environment (i.e., CO and H_2 shown in H_2-TPR), the depletion of O_{lat} is much easier.

Competition between CO-SCR and CO + O_2 oxidation occurs in the 3%O_2 + 10% CO + 500 ppm NO/N_2 atmosphere (Fig. 9b), where the latter becomes dominant. When the furnace temperature reaches the ignition temperature (T_{50}, CO conversion > 10%), as the oxidation rate increases, the local temperature of the catalyst surface increases rapidly, which further promotes the oxidation reaction, resulting in self-

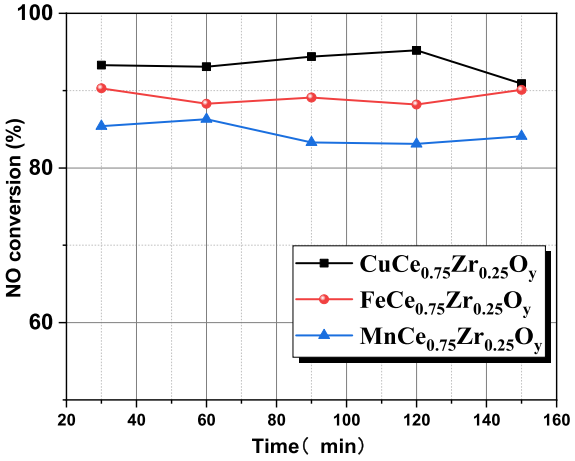

Fig. 10. Catalyst durability test for NO and CO conversions for $CuCe_{0.75}Zr_{0.25}O_y$, $MnCe_{0.75}Zr_{0.25}O_y$, and $FeCe_{0.75}Zr_{0.25}O_y$ catalysts. Conditions: 0% O_2 + 1%CO + 500 ppm NO/N_2 atmosphere, flow rate: 200 mL/min, and weight of catalyst: 0.2 g.

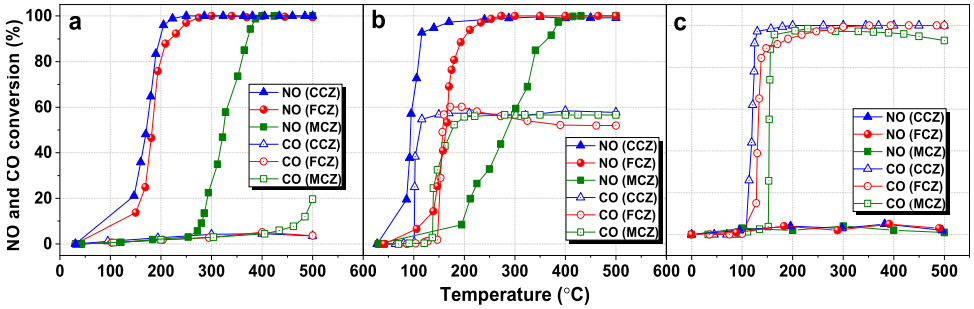

Fig. 9. CO-SCR activity for NO and CO conversions as a function of reaction temperature for $CuCe_{0.75}Zr_{0.25}O_y$, $MnCe_{0.75}Zr_{0.25}O_y$, and $FeCe_{0.75}Zr_{0.25}O_y$ catalysts. Conditions: 0% O_2 + 10% CO + 500 ppm NO/N_2 atmosphere (a); 3%O_2 + 10% CO + 500 ppm NO/N_2 atmosphere (b); and 5% O_2 + 10% CO + 500 ppm NO/N_2 atmosphere (c); flow rate: 200 mL/min; weight of catalyst: 0.2 g.

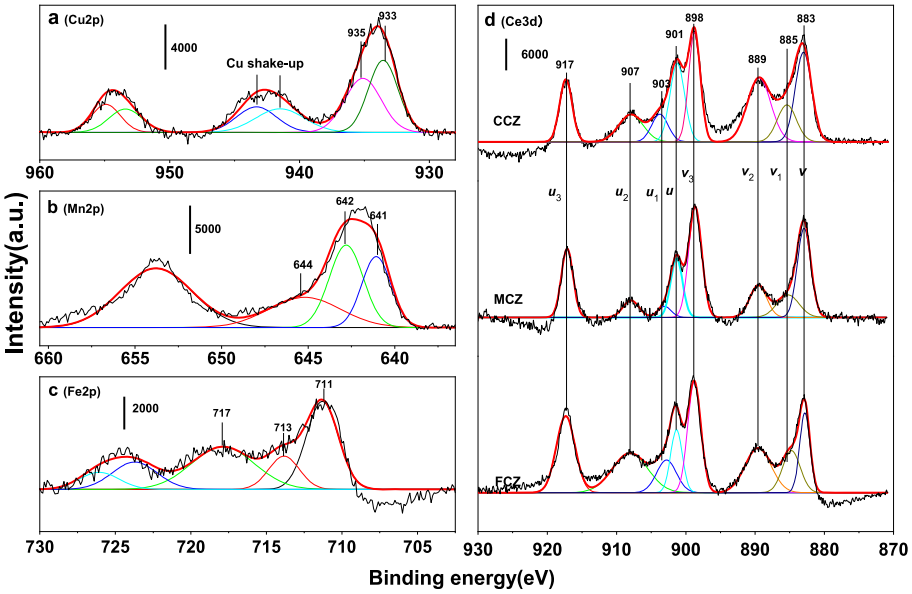

Fig. 11. XPS narrow spectra of Cu 2p (a), Mn 2p (b), Fe 2p (c), and Ce 3d (d) over the spent catalysts. Crude line: original data; Smooth line: fitting data.

sustaining CO combustion on the catalyst surface. Excess CO participates during SCR after complete oxygen consumption because the oxygen content added is below the stoichiometric value of 5% required for CO oxidation. An intense exothermic reaction of CO oxidation results in the temperature of the catalyst bed being higher than the controlled temperature. In this case, for $CuCe_{0.75}Zr_{0.25}O_y$ and $FeCe_{0.75}Zr_{0.25}O_y$, the conversion rate NO rapidly reaches 90% at 114 °C and 190 °C along with CO → CO_2 oxidation, but hysteresis is apparent in the curve for $MnCe_{0.75}Zr_{0.25}O_y$, leading to 90% NO conversion at 361 °C. The oxygen inhibition induced by the consumption of reducing agents is a challenging problem in the reduction of NO by CO over catalysts. When the system is running in the 5% O_2 + 10% CO + 500 ppm NO/N_2 atmosphere (Fig. 9c), most CO is oxidized by O_2, which increases continuously to 100%, 100%, and 98% for $CuCe_{0.75}Zr_{0.25}O_y$, $FeCe_{0.75}Zr_{0.25}O_y$, and $MnCe_{0.75}Zr_{0.25}O_y$, respectively, but CO-SCR appears at a low rate. After the 150 min durability test (Fig. 10), no deactivation was found.

XPS analysis for the spent catalysts is given in Fig. 11. The characteristic peak of Cu $2p_{3/2}$ was fitted by two peaks (Cu^+ at 933 eV and Cu^{2+} at 935 eV.). The Mn $2p_{3/2}$ peak was fitted by three peaks (Mn^{2+} at 641 eV, Mn^{3+} at 642 eV, Mn^{4+} at 644 eV), and the Fe $2p_{3/2}$ spectra were deconvoluted to two peaks (FeO at 711 eV, Fe_3O_4 at 713 eV). The Cu^+: Cu^{2+} atomic ratio increased to 1.08 after the reaction, and manganese existed in the oxidation states of Mn^2, Mn^{3+}, and Mn^{4+} in a 1:1.35:0.78 ratio, proving that Mn^{2+} and Mn^{4+} were mostly converted to Mn^{3+} in the reaction. The XPS spectra of spent catalysts indicate that the Ce^{3+}/Ce^{4+} ratios for $CuCe0_{.75}Zr_{0.25}O_y$, $MnCe0_{.75}Zr_{0.25}O_y$, and $FeCe0_{.75}Zr_{0.25}O_y$ have been changed to 0.17, 0.13, and 0.2, respectively. The changes in the Ce^{3+}/Ce^{4+} ratios for $CuCe0_{.75}Zr_{0.25}O_y$ and $FeCe0_{.75}Zr_{0.25}O_y$ are more obvious than those for $MnCe0_{.75}Zr_{0.25}O_y$, suggesting that the strength of the synergistic effect in Cu-Ce metals and Fe-Ce metals is better than that in Mn-Ce metals. The CO-SCR reaction is a gas–solid surface reaction, and the absorption/desorption of reactants occurs on the atomic/molecular level of metal oxides. To ensure a uniform number of active sites in all catalysts, the same molar ratio of M:Ce:Zr (M = Cu, Mn, Fe) was selected as 4:3:1. Then, the quality of Cu, Fe and Mn is different due to the different molar masses of metals. The proportion of d-π backbonding in CuO increases as the d-electron density of surface active species increases owing to the synergistic effect of Cu-Ce bimetals (the best ratio of Cu:Ce was 1:0.75). Such a phenomenon can improve the ability of the Cu species (Cu^+/Cu^{2+}) to adsorb CO and NO. In brief, the strength of the synergistic effect that is apparent on a macroscopic scale is related to the catalytic performance.

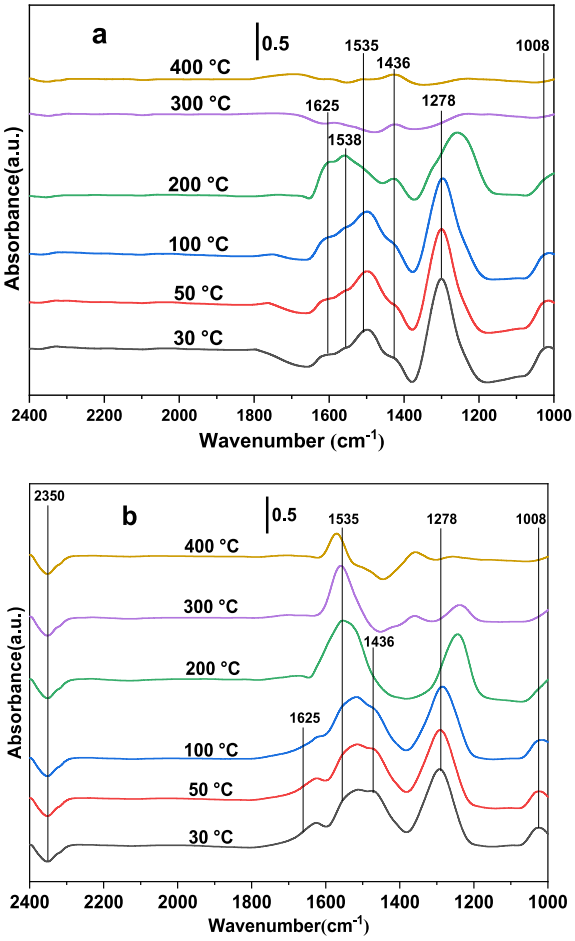

Fig. 12. IR spectra of the (a) $CuCe_{0.75}Zr_{0.25}O_y$ catalyst and (b) $FeCe_{0.75}Zr_{0.25}O_y$. Pretreatment: pure He at 300 °C for 30 min; Sample quality: 20 mg; Experimental conditions: 1% NO + 5% CO + 1% O_2/He (40 mL/min).

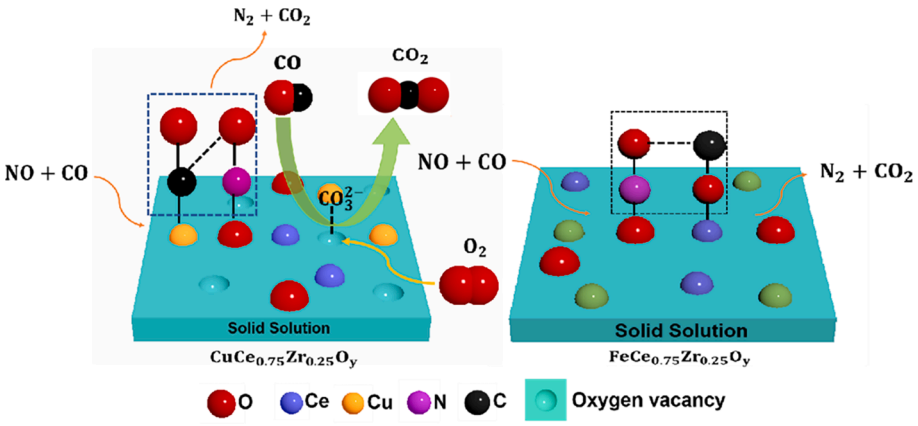

Fig. 13. Possible reaction paths of the CO-SCR reaction on the catalyst surface.

3.6. *In situ IR analysis*

To further understand the adsorption state and reaction intermediate process of CO-SCR and clarify the conversion rule of reaction intermediates, the $CuCe_{0.75}Zr_{0.25}O_y$ catalyst with excellent activity and the $FeCe_{0.75}Zr_{0.25}O_y$ catalyst with moderate activity were selected to carry out in situ IR experiments under different pre-adsorption conditions. The in situ IR spectra in an atmosphere of 1% NO + 5% CO + 1% O_2 are shown in Fig. 12. Fig. 12a shows the spectrum of the $CuCe_{0.75}Zr_{0.25}O_y$ catalyst. The peaks at different positions in the figure are attributed to different intermediate species. The 1008 cm^{-1} peak is attributed to the absorption of monodentate nitrates, the peak at 1278 cm^{-1} is attributed to linear nitrates, the peak at 1535 cm^{-1} is attributed to chelating bidentate nitrates, and the peak at 1625 cm^{-1} is attributed to bridging bidentate nitrates. The intensity of the 1278 cm^{-1} absorption peak is dominant, indicating that NO is mainly present in the form of linear nitrates on the external surface of the catalyst solid solution. The intensities of the peaks at 1008 and 1278 cm^{-1} gradually decrease with increasing temperature. The intensity of the peak at 1535 cm^{-1} remains stable, although it is small at 400 °C, which confirms that the stability of chelated bidentate nitrates on the catalyst surface is higher than that of other forms of nitrates. When NO evident conversion takes place on the catalyst surface at 400 °C, the main intermediate species left are linear nitrate and bridged bidentate nitrates [38–40]. When CO is adsorbed on the $CuCe_{0.75}Zr_{0.25}O_y$ catalyst surface, the monodentate carbonates represented by the peak at 1436 cm^{-1} and the bidentate carbonates represented by the peak at 1538 cm^{-1} are the main intermediate species [41]. The increase in temperature leads to a rapid decrease in the bidentate carbonate absorption peak that disappears at 300 °C. A weak absorption peak attributed to monodentate ligand CO_3^{2-} at 1436 cm^{-1} remains at 400 °C, which indicates that the intermediate species of CO conversion on the catalyst surface is mainly bidentate CO_3^{2-}, and bidentate CO_3^{2-} is more easily decomposed on the catalyst surface than monodentate CO_3^{2-}. In summary, CO to CO_2 on the $CuCe_{0.75}Zr_{0.25}O_y$ catalyst surface is deduced to have two main paths (Fig. 13): The first route should be that CO chemisorption occurs first on the $CuCe_{0.75}Zr_{0.25}O_y$ surface, which combines with lattice oxygen provided by $CuCe_{0.75}Zr_{0.25}O_y$ to form a carbonate structure (CO_3^{2-}). With the increase of reaction temperature, CO_3^{2-} decomposes into CO_2 and enters the gas phase, and the lattice oxygen defect in the solid solution is filled by the oxygen in the environment to form lattice oxygen. Another route includes selective catalytic reduction of NO by CO. NO combines with oxygen species on the catalyst surface to form an N-O coordination structure, and the CO molecule is adsorbed on copper sites to form a Cu^{n+}–CO complex. As the temperature rises continually, the two intermediate species react to produce N_2 and CO_2 [42,43].

For the $FeCe_{0.75}Zr_{0.25}O_y$ catalyst (Fig. 12b), the absorption peak of chelated nitrate at 1535 cm^{-1} still has an evident intensity at 400 °C, which indicates that the stability of chelated nitrate on $FeCe_{0.75}Zr_{0.25}O_y$ is higher than that of $CuCe_{0.75}Zr_{0.25}O_y$, and the reduction rate of the absorption peak area of linear nitrate at 1278 cm^{-1} is less than that of $CuCe_{0.75}Zr_{0.25}O_y$. This finding can explain why the catalytic activity of $FeCe_{0.75}Zr_{0.25}O_y$ is lower than that of $CuCe_{0.75}Zr_{0.25}O_y$. The peak intensity of carbonates on the surface of $FeCe_{0.75}Zr_{0.25}O_y$ is much lower than that of $CuCe_{0.75}Zr_{0.25}O_y$. Therefore, unlike the conversion path of $CuCe_{0.75}Zr_{0.25}O_y$, CO mainly binds to Ce^{3+} on the surface of $FeCe_{0.75}Zr_{0.25}O_y$ and then further reacts with nitrate on the catalyst surface to convert CO_2 (Fig. 13)[44,45].

4. Conclusion

In this paper, catalysts $CuCe_{0.75}Zr_{0.25}O_y$, $MnCe_{0.75}Zr_{0.25}O_y$ and $FeCe_{0.75}Zr_{0.25}O_y$ were prepared, and their physicochemical properties and catalytic reaction mechanism for selective reduction of NO by CO were studied. CO-SCR reaction experiments were carried out over catalysts $CuCe_{0.75}Zr_{0.25}O_y$, $MnCe_{0.75}Zr_{0.25}O_y$ and $FeCe_{0.75}Zr_{0.25}O_y$. Under the condition of 0% O_2 + 10% CO + 500 ppm NO/N_2, the CO-SCR reaction was dominant due to the O_2-free reaction atmosphere. The temperatures at which 90% (T_{90}) NO conversion by $CuCe_{0.75}Zr_{0.25}O_y$ and $FeCe_{0.75}Zr_{0.25}O_y$ was reached are 200 °C and 223 °C, respectively. The activities of these two catalysts are higher than that of $MnCe_{0.75}Zr_{0.25}O_y$ (T_{90} = 375 °C). The oxygen inhibition induced by the consumption of reducing agents is a challenging problem in the reduction of NO by CO over catalysts. When the fed gas was 5% O_2 + 10% CO + 500 ppm NO/N_2, most CO was oxidized by O_2, which increased continuously to 100%, 100%, and 98% for $CuCe_{0.75}Zr_{0.25}O_y$, $FeCe_{0.75}Zr_{0.25}O_y$, and $MnCe_{0.75}Zr_{0.25}O_y$, respectively, but CO-SCR occurred at a low rate. For the CO-SCR reaction over $CuCe_{0.75}Zr_{0.25}O_y$, linear nitrate and bridged nitrate are the main intermediate species in the NO reduction on the catalyst surface, and the intermediate species of CO oxidation on the catalyst surface is mainly bidentate coordinated CO_3^{2-}. Compared with the two other catalysts, $CuCe_{0.75}Zr_{0.25}O_y$, which has a high lattice oxygen mobility, is more likely to react with NO and CO.

Declaration of Competing Interest

The authors declare that they have no known competing financial interests or personal relationships that could have appeared to influence the work reported in this paper.

Acknowledgment

This work is financially supported by the National Natural Science Foundation of China (51776216), The Science and Technology Development Fund, Macau SAR (File no. 0041/2019/A1 and 0046/2019/AFJ), University of Macau (File no. MYRG2017-00216-FST), University

of Macau (File no. MYRG2018-00192-IAPME).

References

[1] L. Chen, X. Shen, S. Xia, F. Sun, Thermodynamic analyses for recovering residual heat of high temperature basic oxygen gas (BOG) by the methane reforming with carbon dioxide reaction, Energy 118 (2017) 906–913.

[2] F. Bin, X. Wei, T. Li, D. Liu, Q. Hao, B. Dou, Self-sustained catalytic combustion of carbon monoxide ignited by dielectric barrier discharge, P. Combust. Inst. 36 (2017) 4193–4200.

[3] S.P. Du Preez, J.P. Beukes, P.G. Van Zyl, M. Tangstad, L.R. Tiedt, Silicon carbide formation enhanced by in-situ-formed silicon nitride: an approach to capture thermal energy of CO-rich off-gas combustion, Metall. Mater. Trans. B. 49B (2018) 3151–3163.

[4] M. Kirschen, H. Pfeifer, F. Wahlers, H. Mees. Off-gas measurements for mass and energy balances of stainless steel EAF, 59th Electric furnace conference, iron and steel society conference proceedings, 2001: 737-745.

[5] M. Kirschen, R. Kühn, S. Lenz, J. Loh, H. Pfeifer, K. Schaefers, F. Wahlers, Off-gas measurements at primary dedusting systems of electric arc furnaces, Stahl und Eisen 124 (2004) 73–89.

[6] M. Kirschen, L. Voj, H. Pfeifer, NO_x emission from electric arc furnace in steel industry: contribution from electric arc and co-combustion reactions, Clean Tech. Environ. Policy 7 (4) (2005) 236–244.

[7] J. Sun, C. Ge, X. Yao, W. Zou, X. Hong, C. Tang, L. Dong. Influence of different impregnation modes on the properties of CuO CeO2/γ-Al2O3 catalysts for NO reduction by CO. Appl. Surf. Sci. 426.dec.31(2017) 279-286.

[8] K. Skalska, J. Miller, S. Ledakowicz, Trends in NO_x abatement: A review, Sci. Total Environ. 408 (2010) 3976–3989.

[9] X. Cheng, X. Bi, Modeling NO_x adsorption onto Fe/ZSM-5 catalysts in a fixed bed reactor, Int. J. Chem. React. Eng. 11 (2013) 1–12.

[10] Y. Pan, B. Shen, L. Liu, Y. Yao, H. Gao, C. Liang, H. Xu, Develop high efficient of NH_3-SCR catalysts with wide temperature range by ball-milled method, Fuel 282 (2020), 118834.

[11] L. Liu, Z. Yao, B. Liu, D. Lin, Correlation of structural characteristics with catalytic performance of CuO/$CexZr_{1-x}O_2$ catalysts for NO reduction by CO, J. Catal. 275 (2010) 45–60.

[12] M. Ogura, A. Kawamura, M. Matsukata, Catalytic activity of Ir for NO-CO reaction in the presence of SO_2 and excess oxygen, Chem. Lett. 29 (2000) 146–147.

[13] Y. Doi, M. Haneda, Catalytic performance of supported Ir catalysts for NO reduction with C_3H_6 and CO in slight lean conditions, Catal. Today. 303 (2018) 8–12.

[14] H. Inomata, M. Shimokawabe, A. Kuwana, M. Arai, Selective reduction of NO with CO in the presence of O_2 with Ir/WO3 catalysts: influence of preparation variables on the catalytic performance, Appl. Catal. B-Environ. 84 (2008) 783–789.

[15] J. Meng, F. Gao, X. Tang, H. Yi, Y. Zhou, Review of the Ir-based catalyst in selective catalytic reduction of NO with CO, Chem. Ind. & Eng. Pro. 38 (2019) 2746–2755.

[16] L. Wang, X. Cheng, Z. Wang, C. Ma, Y. Qin, Investigation on Fe-Co binary metal oxides supported on activated semi-coke for NO reduction by CO, Appl. Catal. B-Environ. 201 (2017) 636–651.

[17] G. Zahra, L. Guohua. Low-Temperature Selective Catalytic Reduction of NO by CO in the Presence of O2 over Cu:Ce Catalysts Supported by Multiwalled Carbon Nanotubes. Ind. Eng. Chem. Res. 57 (2018) acs.iecr.8b01343-.

[18] J. Chen, Y. Chen, M. Zhou, Z. Huang, J. Gao, Z. Ma, X. Tang, Enhanced Performance of Ceria-Based NO_x Reduction Catalysts by Optimal Support Effect, Environ. Sci. Technol. 51 (2017) 473–478.

[19] H. Zhu, J. Kim, S. Ihm, Selective catalytic reduction of NO with CO on Pt/W-Ce-Zr catalysts, React. Kinet. Catal. Lett. 97 (2009) 207–215.

[20] L. Liu, Z. Yao, B. Liu, D. Lin, Correlation of structural characteristics with catalytic performance of CuO/Ce_xZr_1 $_xO2$ catalysts for NO reduction by CO, J. Catal. 275 (2010) 45–60.

[21] L. Guo, T. Zhang, H. Chang, J. Li, Study on Ce-doped Ni-Al-O_x catalysts for reduction by CO, China Environmenal Science 38 (2018) 3313–3321.

[22] H. Li, Dong, B. Zhang, J. Tang. Influence of CeO2 modification on the properties of Fe2O3-Ti0.5Sn0.5O2 catalyst for NO reduction by CO. Catal. Sci. Technol 4 (2914) 482-493.

[23] F. Bin, X. Wei, B. Li, K.S. Hui, Self-sustained combustion of carbon monoxide promoted by the Cu-Ce/ZSM-5 catalyst in $CO/O_2/N_2$ atmosphere, Appl. Catal. B-Environ. 162 (2015) 282–288.

[24] X. Cheng, X. Zhang, D. Su, Z. Wang, J. Chang, C. Ma, NO reduction by CO over copper catalyst supported on mixed CeO_2 and Fe_2O_3: catalyst design and activity test, Catal. B-Environ. 239 (2018) 485–501.

[25] L. Kong, J. Miao, M. Li, G. Tan, G. Jin, Performances of Selective Catalytic Reduction of NO with CO over CuMnCeLa-O/γ-Al_2O_3 Catalyst, J. Mol. Catal. 32 (2018) 295–304.

[26] H. Wan, D. Li, Y. Dai, Y. Hu, B. Liu, L. Dong, Catalytic behaviors of CuO supported on Mn_2O_3 modified gamma-Al_2O_3 for NO reduction by CO, J. Mol Catal A-Chem. 332 (2010) 32–44.

[27] S. Li, Q. Hao, R. Zhao, D. liu, H. Duan, B. Dou. Highly efficient catalytic removal of ethyl acetate over Ce/Zr promoted copper/ZSM-5 catalysts. Chem. Eng. J. 285 (2016) 536-543.

[28] C. Deng, M. Li, J. Qian, Q. Hu, M. Huang, Q. Lin, A study of different doped metal cations on the physicochemical properties and catalytic activities of Ce20M1Ox (M=Zr, Cr, Mn, Fe Co, Sn) composite oxides for nitric oxide reduction by carbon monoxide, Chem-Asian. J. 11 (2016) 2144–2156.

[29] H. Liu, Y. Wang, A. Jia, S. Wang, M. Luo, J. Lu, Oxygen vacancy promoted CO oxidation over Pt/CeO_2 catalysts: a reaction at Pt-CeO_2 interface, Appl. Surf. Sci. 314 (2014) 725–734.

[30] G. Liu, R. Yue, Y. Jia, N. Yong, Y. Jie, H. Liu, Catalytic oxidation of benzene over Ce-Mn oxides synthesized by flame spray pyrolysis, Particuology 11 (2013) 454–459.

[31] J. Zhu, C. Feng, J. Zhang, H. Chen, M. Anpo, Fe^{3+}-TiO_2 photocatalysts prepared by combining sol-gel method with hydrothermal treatment and their characterization, J. Photoch Photobio. A. 180 (2006) 196–204.

[32] W. Yu, Q. Zhou, H. Wang, Y. Liu, W. Yang, Selective removal of CO from hydrocarbon-rich industrial off-gases over CeO_2-supported metal oxides, J. Mater. Sci. 55 (2020) 2321–2332.

[33] F. Meshkini, M. Taghizadeh, M. Bahmani, Investigating the effect of metal oxide additives on the properties of Cu/ZnO/Al_2O_3 catalysts in methanol synthesis from syngas using factorial experimental design, Fuel 89 (2010) 170–175.

[34] P. Wang, C. Cui, K. Li, J. Yi, L. Lei, The effect of Mn content on catalytic activity of the Co-Mn-Ce catalysts for propane oxidation: Importance of lattice defect and surface active species, Catal. Lett. 150 (2020) 1505–1514.

[35] G. Lu, R. Wang, Roles of Ceria on Copper and Manganese Oxides Catalyst-Adsorption of NO and CO, J. Rare. Earth. 4 (1993) 263–268.

[36] P. Li, G. Lu, X. Zhao, W. Xiao, Effect of SO_2 on NO Catalytic Oxidation Studied by TPD Method, Chinese J. Catal. 24 (2003) 681–686.

[37] B. Chen, Y. Ma, L. Ding, L. Xu, Z. Wu, XPS and TPD study of NO interaction with Cu (111): Role of different oxygen species, Chinese J. Catal. 34 (2013) 964–972.

[38] X. Yao, Y. Xiong, W. Zou, L. Zhang, S. Wu, Correlation between the physicochemical properties and catalytic performances of CexSn1-xO_2 mixed oxides for NO reduction by CO, Appl. Catal. B-Environ. 144 (2014) 152–165.

[39] Y. Zhang, L. Zhao, J. Duan, S. Bi, Insights into deNO_x processing over Ce-modified Cu-BTC catalysts for the CO-SCR reaction at low temperature by in situ DRIFTS, Sep. Purif. Technol. 234 (2019), 116081.

[40] X. Cheng, Y. Cheng, Z. Wang, C. Ma, Comparative study of coal based catalysts for NO adsorption and NO reduction by CO, Fuel 214 (2018) 230–241.

[41] H. Liu, L. Liu, L. Wei, B. Chu, Z. Qin, Preparation of three-dimensionally ordered macroporous MFe_2O_4 (M=Co, Ni, Cu) spinel catalyst and its simultaneous catalytic application in CO oxidation and NO+CO reaction, Fuel 272 (2020), 117738.

[42] R. Kang, X. Wei, F. Bin, Z. Wang, Q. Hao, B. Dou, Reaction mechanism and kinetics of CO oxidation over a CuO/$Ce_{0.75}Zr_{0.25}O_2$-delta catalyst, Appl. Catal. A-Gen. 565 (2018) 46–48.

[43] R. Kang, P. Ma, J. He, H. Li, F. Bin, X. Wei, B. Dou, K. Hui, K. Hui, Transient behavior and reaction mechanism of CO catalytic ignition over a CuO–CeO2 mixed oxide, Proceedings of the Combustion Institute 38 (2021) 6493–6501.

[44] S. Li, Theoretical Study of CO, NO Adsorption on Ce(111) Surfaces, Guangzhou Chemical Industry 46 (2018) 18–20.

[45] B. Cheng, Y. Wang, Y. Huang, K.V. Heal, The performance of nitrate-reducing fe(ii) oxidation processes under variable initial Fe/N ratios: the fate of nitrogen and iron species, Front. Env. Sci. Eng. 15 (2021) (2021) 1–12.